Composite Structures 280 (2022) 114952

Contents lists available at ScienceDirect

Composite Structures

journal homepage: www.elsevier.com/locate/compstruct

Temperature-dependent mechanical response of 4D printed composite lattice structures reinforced by continuous fiber

Chengjun Zeng [a], Liwu Liu [a], Wenfeng Bian [b], Jinsong Leng [c], Yanju Liu [a,*]

[a] Department of Astronautical Science and Mechanics, Harbin Institute of Technology (HIT), No. 92 West Dazhi Street, PO Box 301, Harbin 150001, People's Republic of China
[b] Department of Civil Engineering, Harbin Institute of Technology (HIT), Weihai 264209, People's Republic of China
[c] Center for Composite Materials and Structures, Harbin Institute of Technology (HIT), No. 2 YiKuang Street, Harbin 150080, People's Republic of China

ARTICLE INFO

Keywords:
4D printing
Continuous fiber
Lattice structure
Shape memory
Relaxation behavior

ABSTRACT

Four-dimensional (4D) printing endows three-dimensional (3D) objects with structural customizability and functional tunability, which offers the potential to manufacture advanced equipment and devices for specific structural or functional requirements. Here, we investigated the temperature-dependent mechanical and shape memory properties of 4D printed continuous fiber reinforced composite horseshoe lattice structures (CFRCHLSs). Rectangular modified CFRCHLSs with diverse cell configurations were designed and prepared by fiber/matrix co-extrusion process utilizing continuous fibers and shape memory polymer (SMP). Isothermal compression experiments and thermo-mechanical cycle experiments were conducted to investigate the temperature-dependent mechanical properties and thermally-induced active deformation capabilities of 4D printed CFRCHLSs. The results indicate that 4D printed CFRCHLSs possess temperature-dependent equivalent stiffness and peak load, and exhibit shape recovery capabilities affected by geometric configuration. Furthermore, multi-step relaxation experiments were carried out, which revealed the relaxation phenomenon of 4D printed CFRCHLSs at continuous multiple displacements. This work provides guidance for structural design, integrated preparation and characterization of thermodynamic properties of fiber reinforced composite lightweight structures with intelligent deformation behavior.

1. Introduction

Advanced structural materials with characteristics such as light weight, intelligence, high stiffness/strength and energy absorption capabilities are becoming critical for multi-functional applications in aerospace, marine engineering, biomedicine and automotive engineering [1]. Continuous fiber-reinforced composite lightweight structures (CFRCLSs) perfectly integrate these characteristics and present new advances in the tailorability of mechanical properties, so that they are becoming excellent candidates for advanced structural and functional materials. Some CFRCLSs with optimized microstructure design have been proposed, and their corresponding advantages have also been extensively investigated [2–7]. For example, Schneider et al. [4] prepared novel carbon fiber and poly-ethylene terephthalate fiber composite lattice structures with competitive mechanical properties through thermoforming and hot-plate bonding methods. Du et al. [5] fabricated fiber-reinforced foldcores based on curved-crease origami through the prepreg hot press molding process, and investigated the compression performance of the foldcores analytically and experimentally. Pehlivan et al. [6] used the corrugation method to manufacture carbon fiber reinforced composite honeycomb structures with diverse unit configurations, and comprehensively investigated the compression response and energy absorption capabilities of these honeycomb structures. Chen et al. [7] designed a glass fiber reinforced multi-layer composite corrugated sandwich structure and investigated the compression failure mode of the structure numerically and experimentally.

Different from traditional processing methods, additive manufacturing (also known as 3D printing) based on continuous fibers and thermoplastic polymers is a convenient way to develop advanced CFRCLSs due to its integrated customization, short manufacturing cycle, low cost and strong adaptability [8–11]. Recently, intensive efforts have been devoted to investigating the process improvement, structural optimization, performance characterization and multifunctional applications of 3D printed CFRCLSs [12–15]. Hou et al. [16] proposed two

* Corresponding author.
E-mail addresses: zeng_cj@hit.edu.cn (C. Zeng), liulw@hit.edu.cn (L. Liu), bianwf@hit.edu.cn (W. Bian), lengjs@hit.edu.cn (J. Leng), yj_liu@hit.edu.cn (Y. Liu).

https://doi.org/10.1016/j.compstruct.2021.114952
Received 11 July 2021; Received in revised form 24 October 2021; Accepted 2 November 2021
Available online 9 November 2021

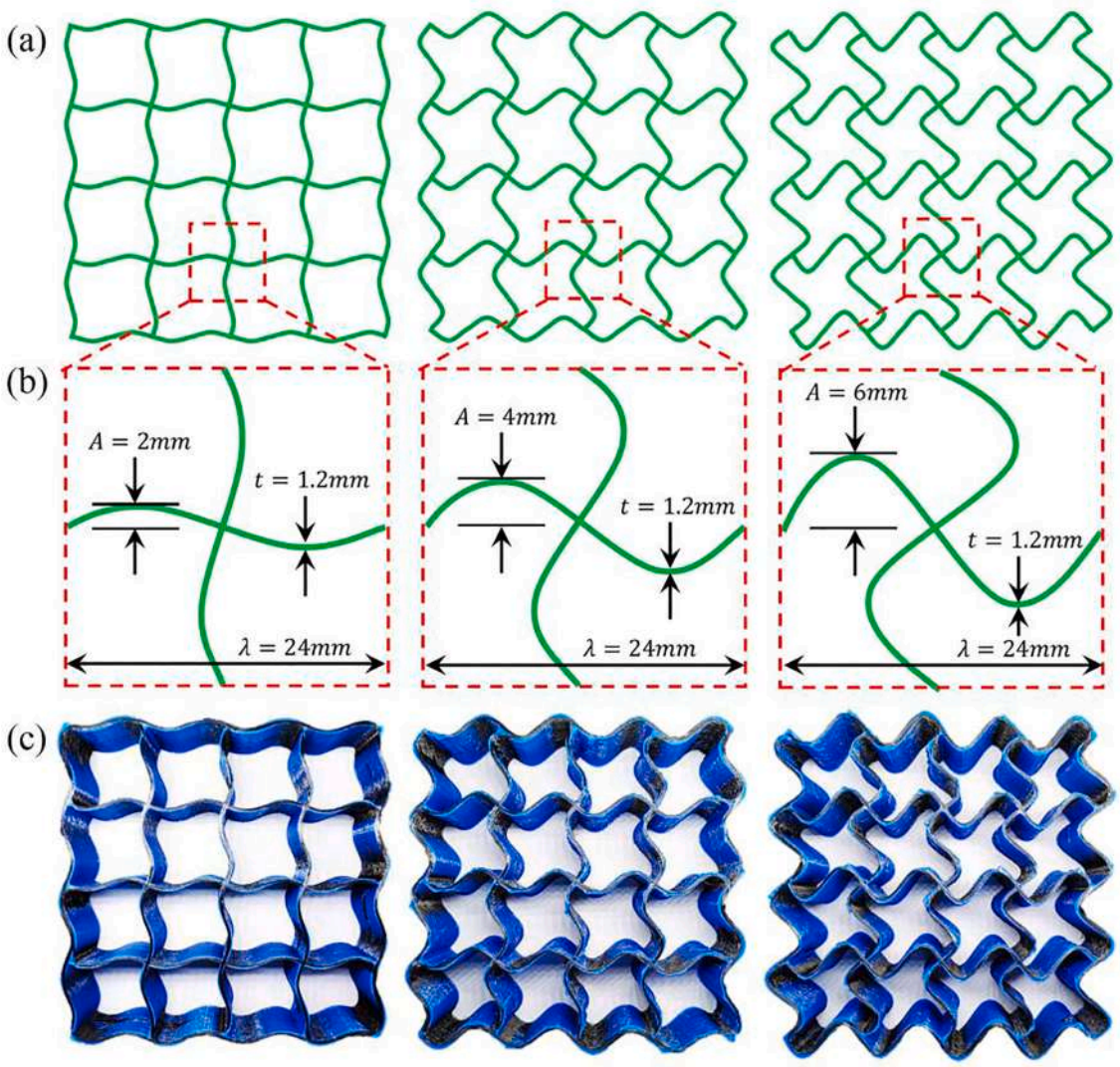

Fig 1. (a) Two-dimensional illustrations for horseshoe lattice structures with various sinusoidal wave amplitudes, (b) representative unit cells of each structure and (c) the corresponding samples manufactured by 4D printing.

design strategies including cross lap and panel-core lap to fabricate CFRCLSs, which preliminarily demonstrated the feasibility of manufacturing CFRCLSs through a 3D printing process. Sugiyama et al. [17] prepared composite sandwich structures with different core configurations utilizing fiber tension and quantified the functional properties of these sandwich structures through three-point bending experiments. Eichenhofer et al. [18] introduced a continuous lattice fabrication method based on additive manufacturing technology for fiber-reinforced ultra-lightweight composite structures. Quan et al. [19] manufactured thermoplastic composite auxetic honeycomb structures with negative Poisson's ratio through 3D printing according to a specific printing path design and investigated the effective stiffness and Poisson's ratio of the structure through analytical and numerical methods. Dong et al. [20] proposed a new 3D printing strategy to fabricate continuous fiber reinforced diamond cellular structures, which can make continuous fiber have good orientation in the cellular structure. Despite these advances, the design and manufacture of programmable, reconfigurable and mechanically tunable intelligent composite lightweight structures remain a challenge.

Fortunately, 4D printing technology, which combines the 3D printing process with stimulus-responsive materials, provides an unprecedented way to develop intelligent composite lightweight structures in one step [21–23]. 4D printed objects can adaptively transform their morphology/structure/behavior under external stimuli such as heat, light, electricity or magnetism [24–28]. Thermally-induced shape memory polymers (SMPs) are a kind of typical stimulus-responsive materials, which are characterized by remarkable programmability, shape memory effect and thermo-viscoelasticity [29–33]. Some studies have preliminarily verified the feasibility of applying SMPs to 4D printing of CFRCLSs [34–36]. However, these studies only considered the printing path planning, characterization of basic mechanical properties and preliminary verification of the shape memory effect of 4D printed CFRCLSs. More complex structural designs and more systematic characterization of thermodynamic properties are required to facilitate versatile applications of 4D printed CFRCLSs.

Herein, we presented 4D printed continuous fiber reinforced composite horseshoe lattice structures (CFRCHLSs) and experimentally investigated their temperature-dependent thermodynamic behavior. The CFRCHLSs were fabricated by fused filament fabrication (FFF) process with continuous carbon fibers and polylactic acid (PLA)-based SMP. The isothermal compression experiments at several temperatures were performed to capture the temperature-dependent mechanical behavior of the CFRCHLSs, and the thermo-mechanical cycle experiments were conducted to evaluate their shape memory properties. The proposed 4D printed CFRCHLSs show significant temperature-dependent compression properties and remarkable shape memory

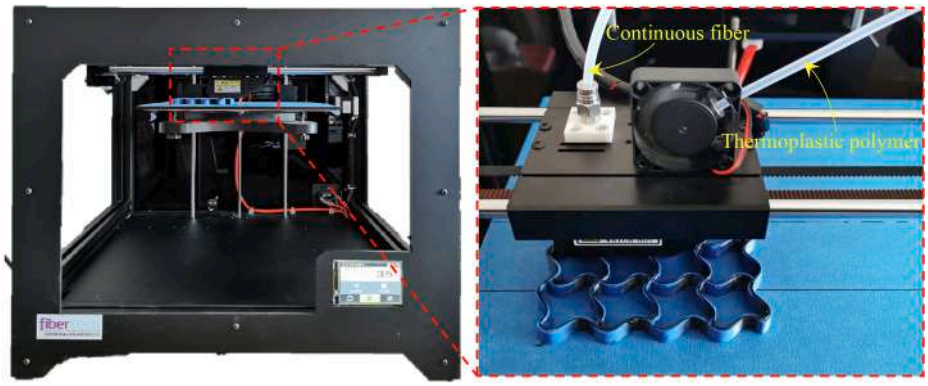

Fig 2. 3D printing device in a co-extrusion manner for the fabrication of CFRCHLSs.

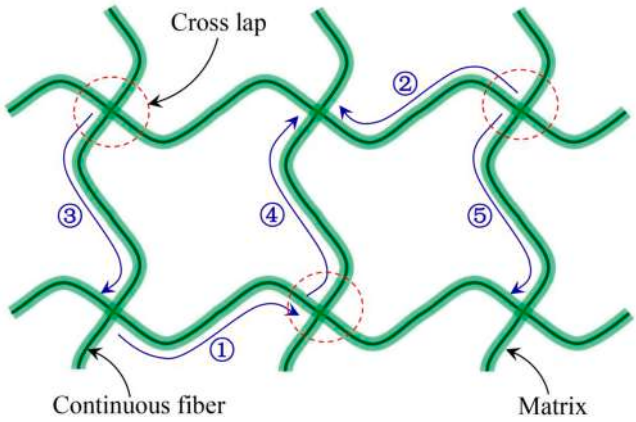

Fig 3. Printing path scheme and cross lap printing strategy.

capabilities. Besides, the multi-step relaxation experiments were conducted to reveal the relaxation behavior of 4D printed CFRCHLSs at multiple displacements.

2. Materials and methods

2.1. Model design

Rectangular modified lattice structures shown in Fig. 1a are designed, which are constructed by replacing the straight connecting beams in the rectangular lattice with horseshoe microstructures [37]. In this study, horseshoe microstructures can be described by periodic sinusoidal waves as [38]

$$y = A \cdot sin\left(\frac{2\pi}{T} \cdot x\right) \tag{1}$$

where A is the sinusoidal wave amplitude and T is the sinusoidal wave period. Three kinds of modified horseshoe lattice structures with diverse configurations are designed by adjusting the sinusoidal wave amplitude. It should be emphasized that the horseshoe lattice structures involved in this study are periodic, and the representative unit cells of various structures are presented in Fig. 1b. The representative unit cells can be described by three structural parameters: sinusoidal wave amplitude A, wavelength λ and wall thickness t. The three types of horseshoe lattice structures have the same wavelength λ and wall thickness t, which are 24 mm and 1.2 mm, respectively. Three different sinusoidal wave amplitudes (i.e., A = 2 mm, 4 mm and 6 mm) are considered.

2.2. Sample fabrication

Based on the geometric models designed in Section 2.1, the FFF-based co-extrusion process was applied to manufacture CFRCHLSs. Fig. 2 shows the continuous fiber reinforced composite 3D printer (Combot-200) from Shaanxi Fibertech Technology Development Co., Ltd., China, which was used for the fabrication of CFRCHLSs in this study. The printer is designed based on the principle of fiber/matrix co-extrusion. Continuous fiber bundle and thermoplastic polymer are fed into the extruder through separated channels and then extruded from the same nozzle. During the preparation of the sample, the in-plane motion path of the printer nozzle is aligned with the tangential direction of the lattice wall. Fig. 3 illustrates the in-plane printing path scheme. The printer nozzle moves in the sequence of the serial number, and the blue curved arrows indicate the in-plane movement direction of the nozzle. It is worth noting that the cross lap strategy is used to enhance the bonding properties between the crossed curved beams of the lattice structure. As shown in Fig. 3, when the nozzle passes through the intersection marked by the red dashed circle, the matrix is melted again and the deposition line is bonded at the intersection, thereby achieving a strong interface bonding.

The long fiber bundle used in this study was Toray T300B-1000-50B carbon fiber, which was composed of 1000 carbon fiber filaments with a diameter of about 7 μm. The thermoplastic polymer consumable was PLA-based SMP filament with a diameter of 1.75 mm [39]. The thermodynamic properties of the filament were investigated through differential scanning calorimetry (DSC) [39]. Some process parameters probably can affect the thermodynamic properties of 4D printed CFRCHLSs. In the present work, the process parameters for all samples were set as: nozzle temperature of 220 ℃, printing speed of 100 mm/min, layer thickness of 0.3 mm, nozzle diameter of 1 mm and substrate temperature of 60 ℃. In addition, all samples were manufactured by stacking 80 layers, resulting in an out-of-plane thickness of 24 mm. Fig. 1c presents three types of samples with different sinusoidal wave amplitudes.

2.3. Experimental characterization

2.3.1. Isothermal compression experiments

Three kinds of 4D printed CFRCHLSs were subjected to in-plane compression experiments at two isothermal conditions (i.e., 28 °C and 90 °C). The isothermal compression experiments were conducted on a Zwick/Roell testing machine with an environmental chamber, where the ambient temperature was held for 20 min before loading to allow for uniformity of temperature in the sample. The loading rate of all experiments was controlled to 4 mm/min following ASTM standard D1621, and the loading continued until densification started. At least three tests were conducted for each type of sample to ensure repeatability. In order to obtain the compression failure mode of the sample, a camera was used

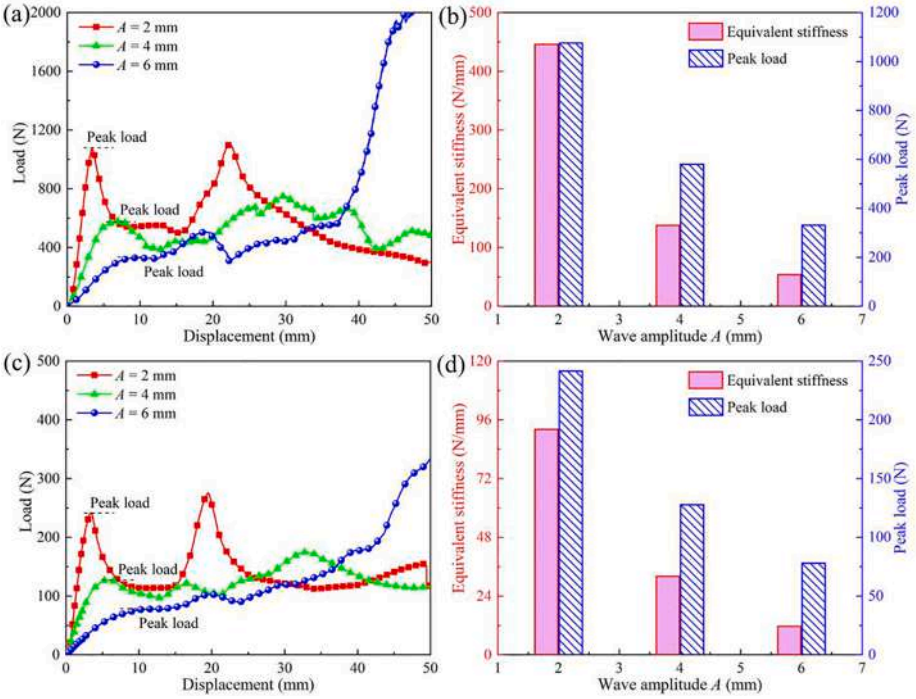

Fig 4. The isothermal compression properties of 4D printed CFRCHLSs with various sinusoidal wave amplitudes. (a) Displacement-load curves at 28 °C. (b) Equivalent stiffness and peak load at 28 °C. (c) Displacement-load curves at 90 °C. (d) Equivalent stiffness and peak load at 90 °C.

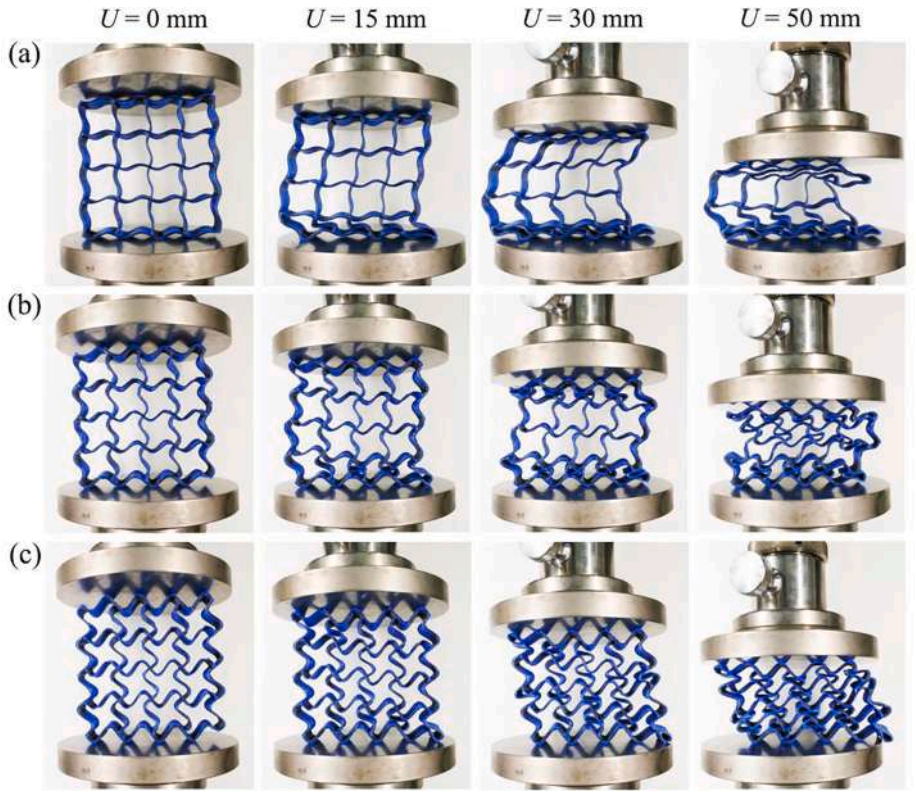

Fig 5. Compression deformation process of 4D printed CFRCHLSs with various sinusoidal wave amplitudes at an isothermal environment of 28 °C. (a) $A = 2$ mm. (b) $A = 4$ mm. (c) $A = 6$ mm.

to track the deformation process of the sample during the experiment.

2.3.2. *Thermo-mechanical cycle experiments*

The shape memory effect of 4D printed CFRCHLSs was investigated by thermo-mechanical cycle experiments, which were performed in compression loading mode on a Zwick/Roell testing machine. The entire thermo-mechanical cycle experiment is divided into the following four steps. Step 1: The sample is first heated to 90 °C at a heating rate of 5 °C/

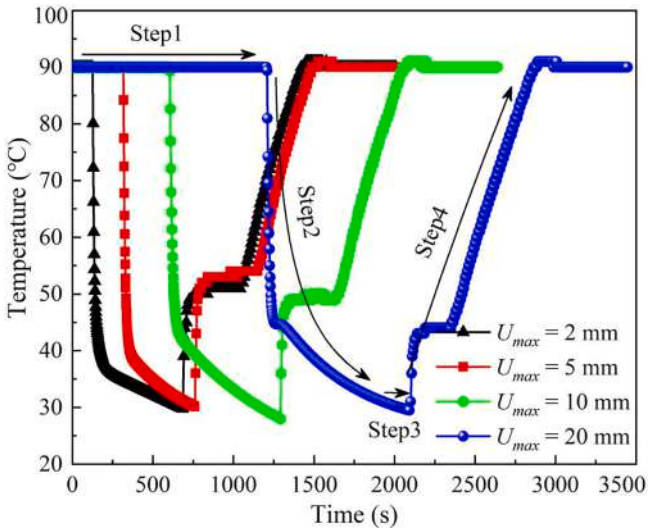

Fig 6. Temperature histories in the thermo-mechanical cycle experiments.

min, and then a maximum displacement U_{max} is applied at a loading rate of 1 mm/min. The influence of different maximum displacement U_{max} on the shape recovery capability of 4D printed CFRCHLSs needs to be investigated, so four maximum loading displacements (i.e., U_{max} = 2, 5, 10 and 20 mm) are set. Step 2: The maximum displacement is maintained, and the temperature is reduced from 90 °C to 28 °C. It should be pointed out that the cooling rate is not constant due to the limitation of the temperature-controlled chamber. Step 3: The temperature is maintained at 28 °C and the load is removed. Step 4: While keeping no load, the temperature is again raised to 90 °C. The experimental data such as compression load, compression displacement and temperature were recorded throughout the test.

2.3.3. *Multi-step relaxation experiments*

Stress relaxation is a typical mechanical characteristic of thermo-viscoelastic polymers and their composites. When a device made of thermo-viscoelastic material is subjected to constant or multi-step strain, it will undergo stress relaxation. Therefore, multi-step relaxation experiments at 28 °C and 65 °C were carried out to evaluate the relaxation behavior of 4D printed CFRCHLSs. The displacements of 1 mm, 2 mm, 5 mm, 10 mm and 20 mm were applied step by step, and each displacement was kept for 20 min. A minimum of three tests were performed for each sample type to ensure reproducibility.

3. Results and discussion

3.1. *Isothermal compression properties*

Fig. 4a and 4c respectively show the compression displacement-load curves of 4D printed CFRCHLSs at 28 °C and 90 °C. It can be observed that the sample undergoes elastic deformation approximately before the load reaches its initial peak. To evaluate the impact of the sinusoidal wave amplitude on the initial elastic deformation of 4D printed CFRCHLSs, here the equivalent stiffness is defined: *Equivalent stiffness* = $(F_2 - F_1) / (U_2 - U_1)$, where U_1, F_1, U_2 and F_2 are the components of the two data points (U_1, F_1) and (U_2, F_2) taken from the initial elastic section of the displacement-load curve. Fig. 4b and 4d summarize the equivalent stiffness and the initial peak load of 4D printed CFRCHLSs under isothermal conditions of 28 °C and 90 °C, respectively. It can be found that the initial peak load and equivalent stiffness decrease significantly with the increase of sinusoidal wave amplitude at both high and low temperature conditions. Moreover, the ambient temperature also has a considerable impact on the initial elastic properties. For example, the initial peak load and equivalent stiffness at 90 °C are 77.5% and 79.3%

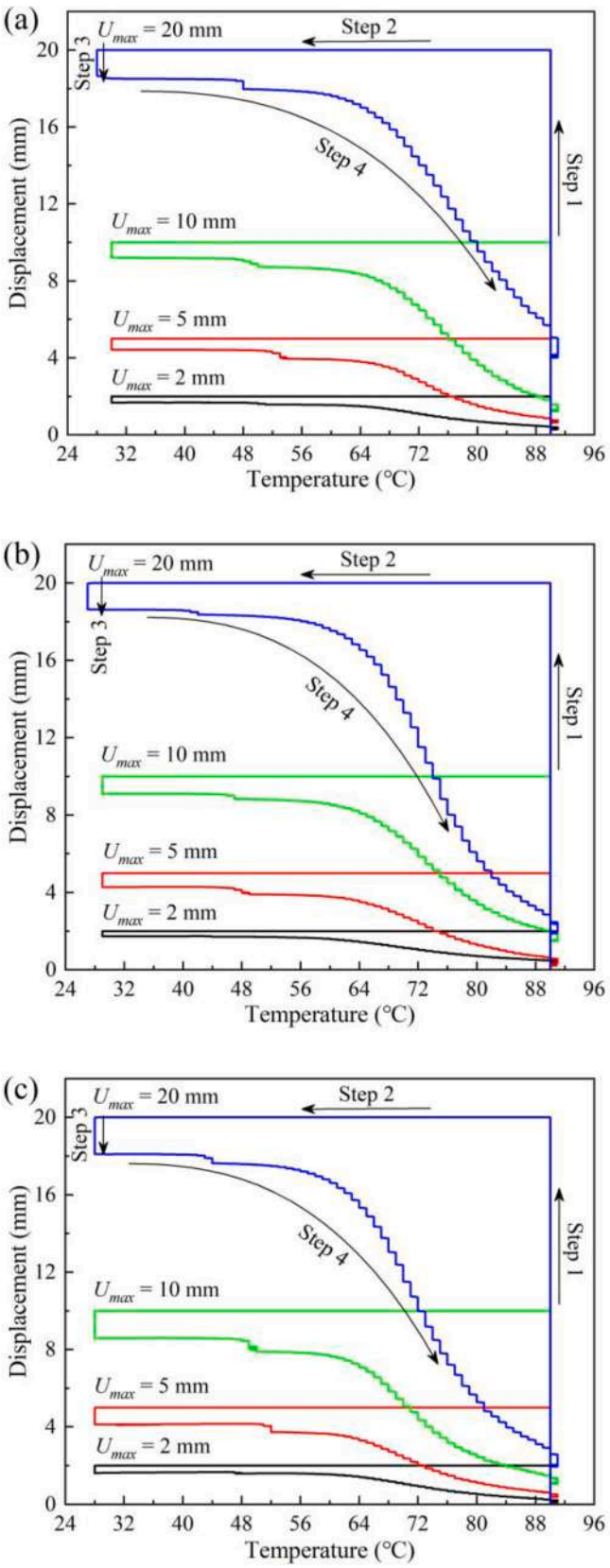

Fig 7. Temperature-displacement plots for the cases (a) A = 2 mm, (b) A = 4 mm and (c) A = 6 mm in the thermo-mechanical cycle experiments.

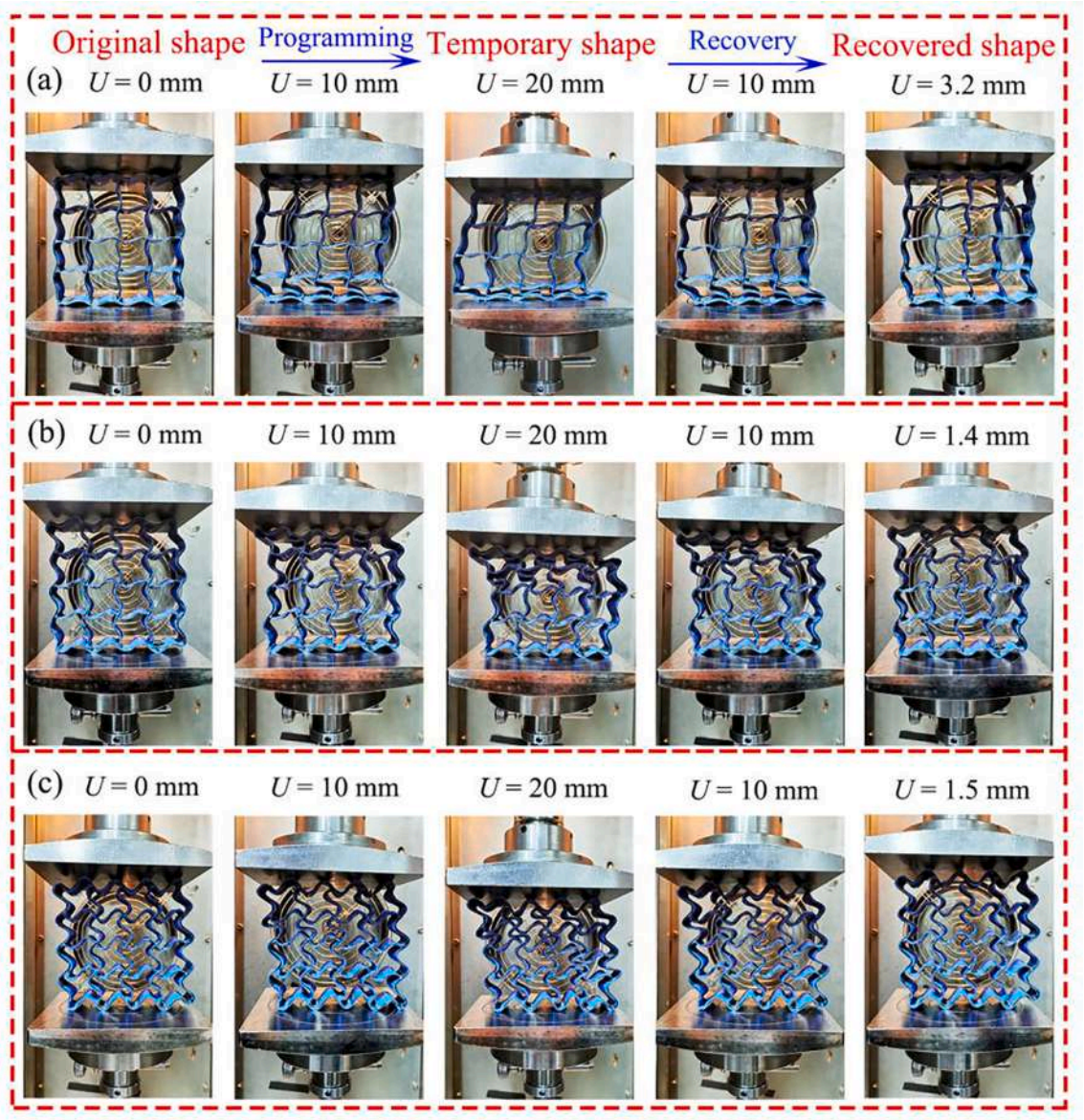

Fig 8. The shape memory behavior of 4D printed CFRCHLSs with sinusoidal wave amplitude (a) A = 2 mm, (b) A = 4 mm and (c) A = 6 mm during thermo-mechanical cycle experiments.

less than those at 28 °C when the wave amplitude is 2 mm, respectively. After the initial elastic phase, the displacement-load curves turn into an elastic–plastic phase accompanied by fluctuations in the load. It can be noticed from Fig. 4a and 4c that the evolution of this phase tends to become gentler as the sinusoidal wave amplitude increases. In fact, the smaller the sinusoidal wave amplitude of the curved beams of the modified horseshoe lattice is, the more likely it is to buckle under the action of the axial force, which leads to greater load fluctuations.

Fig. 5 presents the snapshots of the compression deformation process of 4D printed CFRCHLSs at an isothermal environment of 28 °C. It can be observed in Fig. 5a that lattices at the bottom of the sample with a sinusoidal wave amplitude of 2 mm have been compacted when the compression displacement is 15 mm. With the further increase of displacement, the load will gradually increase until lattices at the top of the sample yield. Therefore, the displacement-load curves evolve a second load peak within the displacement interval of 15 mm to 25 mm for the sample with a sinusoidal wave amplitude of 2 mm as seen in Fig. 4a and 4c. When the wave amplitude is 4 mm, Fig. 5b indicates that the horseshoe cells of the sample rotate during the deformation process, which can slow down the load fluctuation. When the wave amplitude is 6 mm, more uniform deformations are observed in Fig. 5c, which are attributed to the more likely cell rotation caused by the large sinusoidal wave amplitude. It can be seen from Fig. 4a that the displacement-load curve of the sample with a wave amplitude of 6 mm has entered the densification phase earlier than those of the samples corresponding to the wave amplitudes of 2 mm and 4 mm. This is because the large sinusoidal wave amplitude causes adjacent cells to come into contact earlier during the compression process, which will significantly increase the magnitude of the load.

3.2. Shape memory properties

Since the matrix material is a PLA-based SMP, 4D printed CFRCHLSs possess shape memory properties. The thermo-mechanical cycle experiments can evaluate the shape fixability and shape recovery characteristics of 4D printed CFRCHLSs. The thermo-mechanical cycle experiments were executed in four steps according to temperature conditions. The curves of temperature variation with time in the

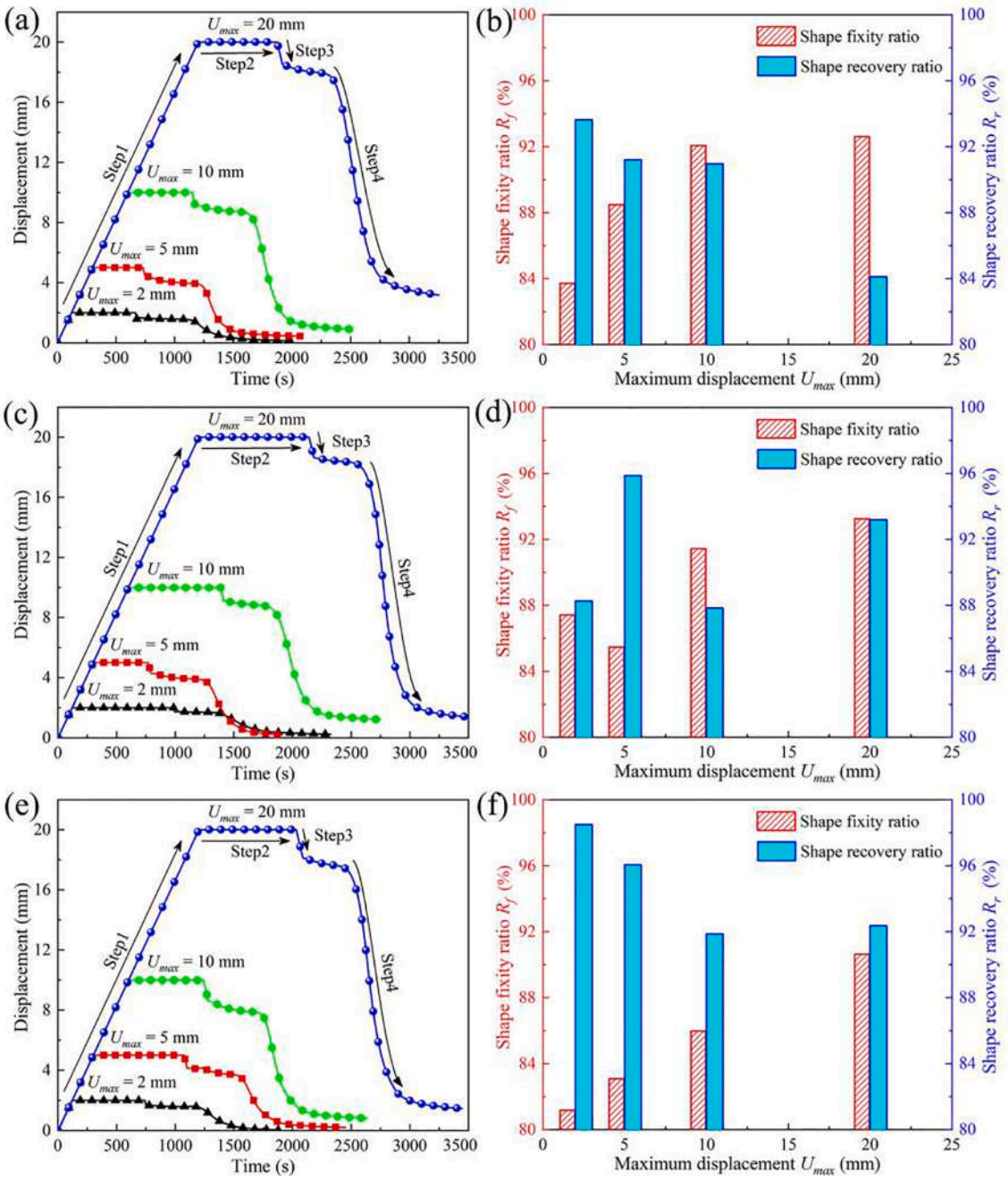

Fig 9. Shape memory effects of 4D printed CFRCHLSs. (a) Time-displacement plots for the case $A = 2$ mm. (b) The effect of the maximum displacement $U_{\max}$ on the shape fixity ratio and shape recovery ratio for the case $A = 2$ mm. (c) Time-displacement plots for the case $A = 4$ mm. (d) The effect of $U_{\max}$ on the shape fixity ratio and shape recovery ratio for the case $A = 4$ mm. (e) Time-displacement plots for the case $A = 6$ mm. (f) The effect of $U_{\max}$ on the shape fixity ratio and shape recovery ratio for the case $A = 6$ mm.

experiments were recorded and displayed in Fig. 6. Limited by the temperature-controlled chamber, the cooling rate in the cooling phase (Step2) exhibited an exponential decrease, and the heating rate in the heating phase (Step4) did not remain constant. The difference in the maximum displacement in the first step led to the difference in the temperature profiles.

Fig. 7 presents the temperature-displacement plots measured in the thermo-mechanical cycle experiments of 4D printed CFRCHLSs with various sinusoidal wave amplitudes, from which the variation of displacement with temperature for different loading steps can be clearly obtained. By observing Fig. 7a, it can be found that the variation of displacement with temperature exhibits a closed loop when the sinusoidal wave amplitude is 2 mm. With the increase of the maximum displacement U_{max}, the temperature-displacement curves show an increased displacement increment in the first step as well as an increased displacement rebound in the third step. The fourth step is the free recovery phase, where the variation of displacement with temperature presents a more complicated trend. At the initial stage of heating, the displacement remains essentially constant. When the temperature reaches 45 °C, the free recovery begins, which is reflected by the reduction of displacement. As the temperature increases to 60 °C, the recovery rate increases significantly. When the ambient temperature reaches 80 °C, the recovery rate decreases slowly. It should be pointed out that the sample has not recovered to its original shape after the temperature is raised to 90 °C. If the temperature is kept at 90 °C, the free recovery process will continue. When the sinusoidal wave amplitude is 4 mm or 6

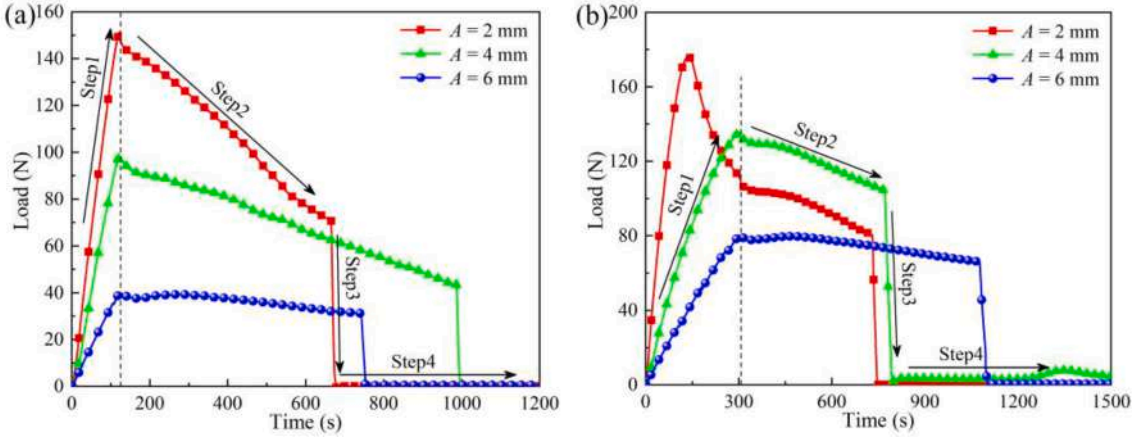

Fig 10. Time-load plots for the cases (a) U_{max} = 2 mm and (b) U_{max} = 5 mm.

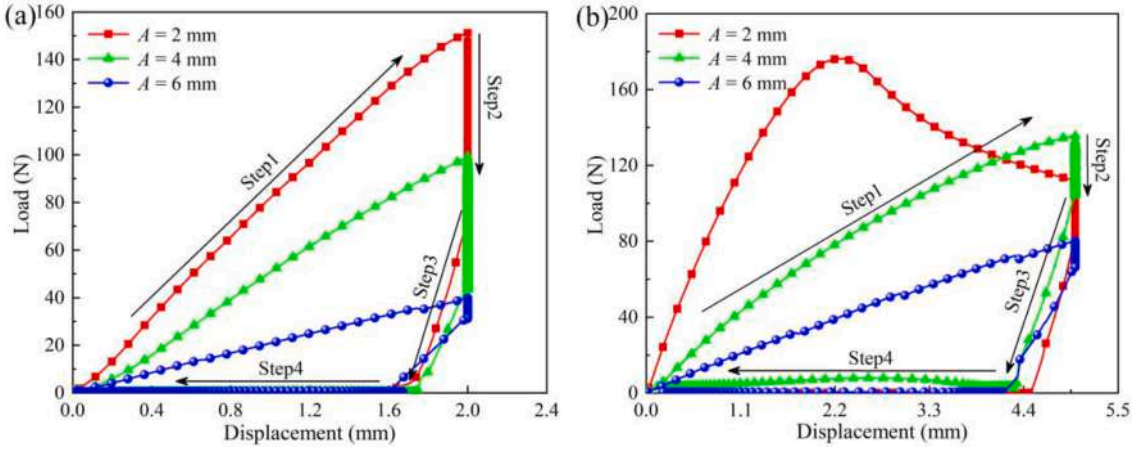

Fig 11. Displacement-load plots for the cases (a) U_{max} = 2 mm and (b) U_{max} = 5 mm.

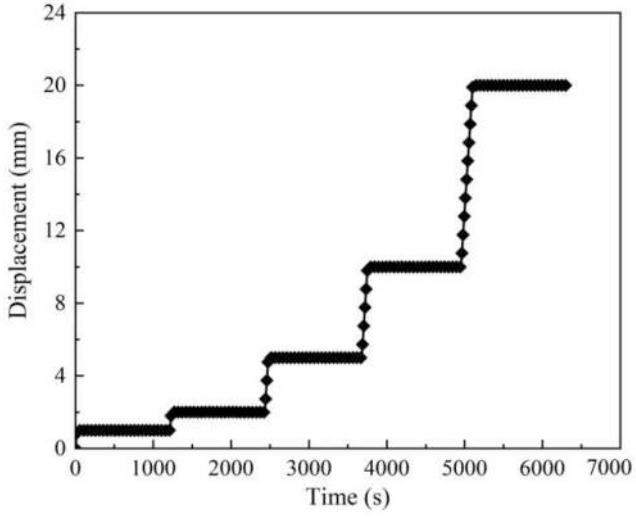

Fig 12. The displacement loading history in the multi-step relaxation experiments.

mm, a conclusion similar to Fig. 7a can be obtained by observing Fig. 7b or 7c.

To visually illustrate the shape memory characteristics of 4D printed CFRCHLSs, Fig. 8 exhibits the programming and free recovery process of the samples with different sinusoidal wave amplitudes in the thermo-mechanical cycle experiments when the maximum displacement U_{max} = 20 mm. During the programming phase, the sample was subjected to a maximum displacement of 20 mm at an isothermal environment of 90 °C. Fig. 8 shows the snapshots of the samples for loading displacements of 0 mm, 10 mm and 20 mm. During the free recovery phase, the ambient temperature was raised to 90 °C while maintaining zero load. To compare with the configurations of the sample in the programming phase, the snapshots of the sample at different displacements in the free recovery phase were also given in Fig. 8. It is worth noting that the recovered shape of the sample is different from the original shape, because the shape recovery ratio does not reach 100%. When the sinusoidal wave amplitude is 2 mm, it can be seen in Fig. 8a that the sample exhibits significant uneven deformation during the programming phase, and the cells at the bottom of the sample yield at the nodes. Nevertheless, the sample still shows excellent shape recovery capability in the free recovery phase. As the sinusoidal wave amplitude increases, the deformation of the sample becomes more and more uniform in the programming phase. For instance, when the sinusoidal wave amplitude is 6 mm, the sample experienced completely uniform deformation, no yielding failure of the sample is observed from the images, and the sample also exhibits excellent shape recovery capability in the free recovery phase.

Furthermore, the shape fixity ratio R_f and the shape recovery ratio R_r are defined to quantify the shape memory properties of 4D printed CFRCHLS:

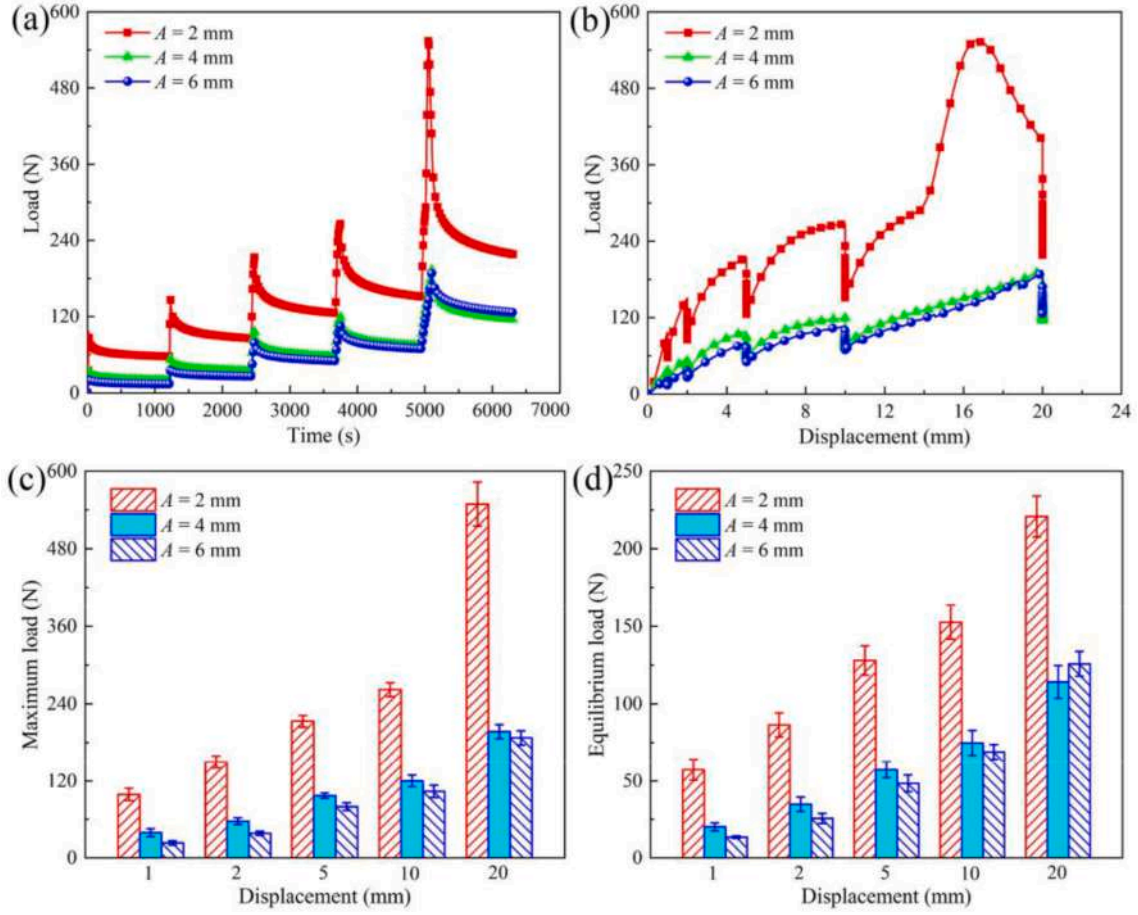

Fig 13. Multi-step relaxation behavior of 4D printed CFRCHLSs at 65 °C. (a) Time vs load plots of samples with various sinusoidal wave amplitudes. (b) Displacement vs load plots of samples with various sinusoidal wave amplitudes. (c) Maximum load in various displacement intervals. (d) Equilibrium load in various displacement intervals.

$$R_f = \frac{U_f - U_0}{U_{max} - U_0} \times 100\% \tag{2}$$

$$R_r = \frac{U_r - U_0}{U_{max} - U_0} \times 100\% \tag{3}$$

where U_0 is the initial displacement before the experiment, $U_0 = 0$ in this paper; U_{max} is the maximum displacement in the first step of the thermo-mechanical cycle experiment; U_f is the displacement of the sample at the beginning of the fourth step; U_r is the displacement of the sample at the end of the fourth step.

Fig. 9 presents the time-displacement curves of 4D printed CFRCHLSs in the thermo-mechanical cycle experiments, as well as the shape fixity ratios and shape recovery ratios obtained from these curves. As can be seen in Fig. 9a, 9c and 9e, the time-displacement curves for all samples exhibit an obvious S-shaped trend in the fourth step of the thermo-mechanical cycle experiment although there are different sinusoidal wave amplitudes and maximum displacements. In addition, both the initial displacement of the sample at the beginning of the fourth step and the residual displacement at the end of the fourth step increase with the increase of the maximum displacement when the sinusoidal wave amplitudes are the same. Fig. 9b, 9d and 9f give the shape fixity ratios and shape recovery ratios of the samples with various maximum displacements for sinusoidal wave amplitudes of 2 mm, 4 mm and 6 mm, respectively.

It can be observed from Fig. 9b that when the wave amplitude is 2 mm, the shape fixity ratios of the samples with maximum displacement U_{max} = 2 mm, 5 mm, 10 mm and 20 mm are 83.7%, 88.5%, 92.1% and 92.6%, respectively, while the corresponding shape recovery ratios are 93.6%, 91.2%, 90.9% and 84.1%. Obviously, the shape fixity ratio is positively correlated with the maximum displacement, and conversely, the shape recovery ratio is negatively correlated with the maximum displacement. The reason why the shape fixity ratios of the samples are less than 100% is that the elastic deformation of the fibers is released in the third step, which is not stored as shape memory strain during the cooling process. Besides, as the maximum compression displacement increases, failures may occur in the composite structures, which will lead to greater residual strains that are difficult to recover. By comparing Fig. 9b, 9d and 9f, it can be found that the sinusoidal wave amplitude also affects the shape fixity ratio and shape recovery ratio of 4D printed CFRCHLSs. For example, when the maximum displacement is 5 mm, the shape fixity ratios for samples with wave amplitudes of 2 mm, 4 mm and 6 mm are 88.5%, 85.5% and 83.1%, respectively, and the corresponding shape recovery ratios are 91.2%, 95.9% and 96.1%, respectively. This indicates that the sample with a wave amplitude of 6 mm possesses the lowest shape fixity ratio, but the highest shape recovery ratio.

Figs. 10 and 11 respectively present the time-load response and displacement-load response of 4D printed CFRCHLSs with different sinusoidal wave amplitudes measured in the thermo-mechanical cycle experiments. When the maximum displacement is 2 mm, it can be found in Fig. 10a and 11a that the maximum load and equivalent stiffness of the sample decrease significantly with increasing sinusoidal wave amplitude in the first step of the experiment, which is consistent with the analysis results in Section 3.1. In the second step of the thermo-mechanical cycle experiment, the load generally decreases as the temperature decreases, which is attributed to the thermal contraction of the

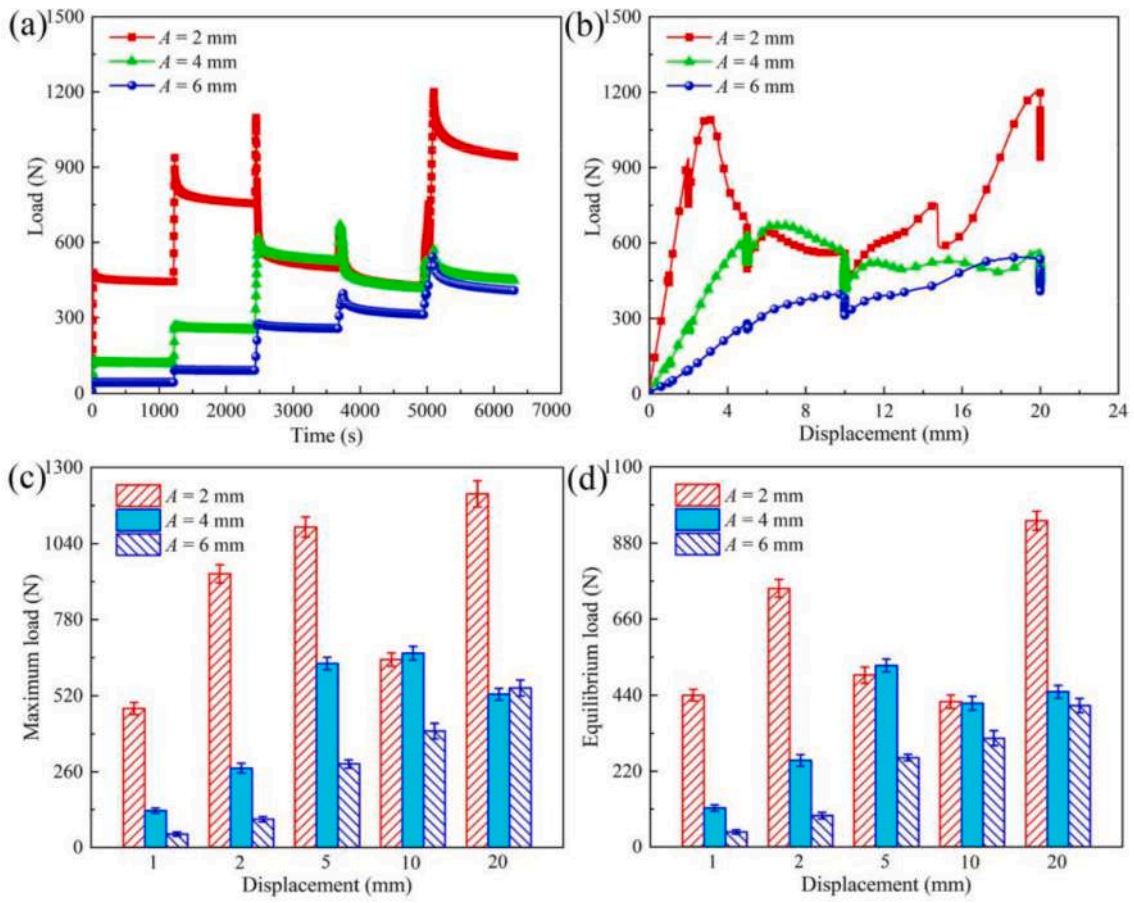

Fig 14. Multi-step relaxation behavior of 4D printed CFRCHLSs at 28 °C. (a) Time vs load plots. (b) Displacement vs load plots. (c) Maximum load in different displacement intervals. (d) Equilibrium load in different displacement intervals.

material caused by the temperature drop. Moreover, as the sinusoidal wave amplitude decreases, the decreasing trend of the load becomes more pronounced. It should be noted that the cooling time of the sample at this phase is different due to the limitation of the temperature-controlled chamber. When the maximum displacement is 5 mm, similar analysis results can be obtained from Fig. 10b and 11b. The difference is that the sample with a wave amplitude of 2 mm yields in the first step of the thermo-mechanical cycle experiment when the maximum displacement is 5 mm.

3.3. Relaxation behavior

In order to quantify the relaxation behavior of 4D printed CFRCHLSs at multiple displacements, multi-step relaxation experiments were conducted, in which incremental displacements were applied. Fig. 12 presents the displacement loading history in the relaxation experiments. The step displacements were applied at intervals of 1 mm, 2 mm, 5 mm, 10 mm and 20 mm. In the multi-step relaxation experiments, the samples were compressed in several consecutive steps and allowed to relax for 1200 s in each step. Fig. 13a and 13b exhibit the time-load and displacement-load curves measured in an isothermal environment at 65 °C, respectively, from which the statistics of the maximum and equilibrium loads for several displacement intervals can be smoothly obtained, which are presented in Fig. 13c and 13d, respectively. When the sinusoidal wave amplitude is 2 mm, the equilibrium loads of the sample in the displacement intervals of 1 mm, 2 mm, 5 mm, 10 mm and 20 mm are 57.3 N, 86.4 N, 128.0 N, 152.7 N and 220.8 N respectively, which is 42.1%, 42.3%, 39.9%, 41.7% and 59.8% less than the peak loads in the corresponding displacement intervals. Obviously, the relaxation behavior of the sample in each displacement interval is similar when the displacement is within 10 mm. When the loading displacement is 20 mm, the relaxation is more pronounced due to the failure of the structure under large deformation. In addition, the sinusoidal wave amplitude also affects the relaxation behavior of 4D printed CFRCHLSs. As seen in Fig. 13d, the samples with sinusoidal wave amplitudes of 4 mm and 6 mm possess similar equilibrium loads in each displacement interval, but these equilibrium loads are significantly lower than those of the sample with a wave amplitude of 2 mm.

Fig. 14 shows the multi-step relaxation response measured in an isothermal environment of 28 °C, which is different from the relaxation response at 65 °C. It can be observed from Fig. 14a and 14d that when the displacement is 5 mm, the equilibrium load of the sample with a sinusoidal wave amplitude of 2 mm is significantly lower than that when the displacement is 2 mm, which is attributed to the plastic deformation and yielding failure of the structure. A similar phenomenon can be observed in the sample with a sinusoidal wave amplitude of 4 mm. When the sinusoidal wave amplitude is 6 mm, the equilibrium load of the sample increases monotonously with the displacement, which means that the sample does not suffer significant plastic deformation and yielding failure during the entire relaxation process.

4. Conclusions

In this contribution, rectangular modified CFRCHLSs with different sinusoidal wave amplitudes were proposed and fabricated by 4D printing. Afterward, several characterization techniques including isothermal compression experiments, thermo-mechanical cycle experiments and multi-step relaxation experiments were applied to investigate the temperature-dependent thermodynamic properties and relaxation behavior of 4D printed CFRCHLSs. The results of isothermal

compression experiments demonstrate that increasing the ambient temperature can significantly reduce the equivalent compression stiffness and the initial peak load of CFRCHLSs, and the equivalent stiffness and initial peak load decrease with increasing sinusoidal wave amplitude at isothermal conditions. The measurements obtained from the thermo-mechanical cycle experiments indicate that 4D printed CFRCHLSs possess the ability to fix their temporary shape and freely recover their original shape, and the shape fixity ratio and shape recovery ratio are positively and negatively related to the maximum displacement, respectively. For instance, when the sinusoidal wave amplitude is 2 mm, the shape fixity ratios of the samples with the maximum displacement $U_{max} = 2$ mm, 5 mm, 10 mm and 20 mm are 83.7%, 88.5%, 92.1% and 92.6%, respectively, while the corresponding shape recovery ratios are 93.6%, 91.2%, 90.9% and 84.1%. In the multi-step relaxation experiments, step displacement was applied at intervals of 1 mm, 2 mm, 5 mm, 10 mm and 20 mm. When the ambient temperature is 65 °C, the sample exhibits similar relaxation behavior at each displacement interval up to 10 mm.

In summary, the proposed 4D printed CFRCHLSs serve as potential candidates for mechanical metamaterials with variable stiffness due to their temperature-dependent mechanical properties. And the remarkable shape memory effect is a feature that can be used to design novel deployable structures and smart morphing devices. Therefore, the findings in this article provide a reliable guideline to novelly develop advanced structural materials for aerospace, marine engineering, biomedicine and automotive engineering.

Declaration of Competing Interest

The authors declare that they have no known competing financial interests or personal relationships that could have appeared to influence the work reported in this paper.

Acknowledgements

This work is supported by the National Natural Science of China (Grant Nos. 11632005, 12072094 and 12172106).

References

[1] Jiang H, Le Barbenchon L, Bednarcyk BA, Scarpa F, Chen Y. Bioinspired multilayered cellular composites with enhanced energy absorption and shape recovery. Addit Manuf 2020;36:101430. https://doi.org/10.1016/j.addma.2020.101430.
[2] Vitale P, Francucci G, Rapp H, Stocchi A. Shear response of ultra-lightweight CFRP cores. Compos Struct 2020;238:111879. https://doi.org/10.1016/j.compstruct.2020.111879.
[3] Wei X, Li D, Xiong J. Fabrication and mechanical behaviors of an all-composite sandwich structure with a hexagon honeycomb core based on the tailor-folding approach. Compos Sci Technol 2019;184:107878. https://doi.org/10.1016/j.compscitech.2019.107878.
[4] Schneider C, Velea MN, Kazemahvazi S, Zenkert D. Compression properties of novel thermoplastic carbon fibre and poly-ethylene terephthalate fibre composite lattice structures. Mater Des 2015;65:1110–20.
[5] Du Y, Song C, Xiong J, Wu L. Fabrication and mechanical behaviors of carbon fiber reinforced composite foldcore based on curved-crease origami. Compos Sci Technol 2019;174:94–105.
[6] Pehlivan L, Baykasoğlu C. An experimental study on the compressive response of CFRP honeycombs with various cell configurations. Compos Part B: Eng 2019;162:653–61.
[7] Chen L, Peng S, Liu J, Liu H, Chen L, Du B, et al. Compressive response of multi-layered thermoplastic composite corrugated sandwich panels: Modelling and experiments. Compos Part B: Eng 2020;189:107899. https://doi.org/10.1016/j.compositesb:2020.107899.
[8] Wang F, Wang G, Ning F, Zhang Z. Fiber–matrix impregnation behavior during additive manufacturing of continuous carbon fiber reinforced polylactic acid composites. Addit Manuf 2021;37:101661. https://doi.org/10.1016/j.addma.2020.101661.
[9] Le Duigou A, Chabaud G, Matsuzaki R, Castro M. Tailoring the mechanical properties of 3D-printed continuous flax/PLA biocomposites by controlling the slicing parameters. Compos Part B: Eng 2020;203:108474. https://doi.org/10.1016/j.compositesb:2020.108474.
[10] Sugiyama K, Matsuzaki R, Malakhov AV, Polilov AN, Ueda M, Todoroki A, et al. 3D printing of optimized composites with variable fiber volume fraction and stiffness using continuous fiber. Compos Sci Technol 2020;186:107905. https://doi.org/10.1016/j.compscitech.2019.107905.
[11] Chacón JM, Caminero MA, Núñez PJ, García-Plaza E, García-Moreno I, Reverte JM. Additive manufacturing of continuous fibre reinforced thermoplastic composites using fused deposition modelling: Effect of process parameters on mechanical properties. Compos Sci Technol 2019;181:107688. https://doi.org/10.1016/j.compscitech.2019.107688.
[12] Diourté A, Bugarin F, Bordreuil C, Segonds S. Continuous three-dimensional path planning (CTPP) for complex thin parts with wire arc additive manufacturing. Addit Manuf 2021;37:101622. https://doi.org/10.1016/j.addma.2020.101622.
[13] Luo M, Tian X, Shang J, Zhu W, Li D, Qin Y. Impregnation and interlayer bonding behaviours of 3D-printed continuous carbon-fiber-reinforced poly-ether-ether-ketone composites. Compos Part A: Appl Sci Manuf 2019;121:130–8.
[14] Caminero MA, Chacón JM, García-Moreno I, Rodríguez GP. Impact damage resistance of 3D printed continuous fibre reinforced thermoplastic composites using fused deposition modelling. Compos Part B: Eng 2018;148:93–103.
[15] Caminero MA, García-Moreno I, Rodríguez GP, Chacón JM. Internal damage evaluation of composite structures using phased array ultrasonic technique: Impact damage assessment in CFRP and 3D printed reinforced composites. Compos Part B: Eng 2019;165:131–42.
[16] Hou Z, Tian X, Zhang J, Li D. 3D printed continuous fibre reinforced composite corrugated structure. Compos Struct 2018;184:1005–10.
[17] Sugiyama K, Matsuzaki R, Ueda M, Todoroki A, Hirano Y. 3D printing of composite sandwich structures using continuous carbon fiber and fiber tension. Compos Part A: Appl Sci Manuf 2018;113:114–21.
[18] Eichenhofer M, Wong JCH, Ermanni P. Continuous lattice fabrication of ultra-lightweight composite structures. Addit Manuf 2017;18:48–57.
[19] Quan C, Han B, Hou Z, Zhang Qi, Tian X, Lu TJ. 3d printed continuous fiber reinforced composite auxetic honeycomb structures. Compos Part B: Eng 2020;187:107858. https://doi.org/10.1016/j.compositesb:2020.107858.
[20] Dong Ke, Liu L, Huang X, Xiao X. 3D printing of continuous fiber reinforced diamond cellular structural composites and tensile properties. Compos Struct 2020;250:112610. https://doi.org/10.1016/j.compstruct.2020.112610.
[21] Chen D, Liu Q, Han Z, Zhang J, Song HongLie, Wang K, et al. 4D Printing Strain Self-Sensing and Temperature Self-Sensing Integrated Sensor-Actuator with Bioinspired Gradient Gaps. Adv Sci 2020;7(13):2000584. https://doi.org/10.1002/advs.v7.1310.1002/advs.202000584.
[22] Ryan KR, Down MP, Banks CE. Future of additive manufacturing: Overview of 4D and 3D printed smart and advanced materials and their applications. Chem Eng J 2021;403:126162. https://doi.org/10.1016/j.cej.2020.126162.
[23] Podstawczyk D, Nizioł M, Szymczyk-Ziółkowska P, Fiedot-Toboła M. Development of Thermoinks for 4D Direct Printing of Temperature-Induced Self-Rolling Hydrogel Actuators. Adv Funct Mater 2021;31(15):2009664. https://doi.org/10.1002/adfm.v31.1510.1002/adfm.202009664.
[24] Zhu P, Yang W, Wang R, Gao S, Li Bo, Li Qi. 4D Printing of Complex Structures with a Fast Response Time to Magnetic Stimulus. ACS Appl Mater Inter 2018;10(42):36435–42.
[25] Xin X, Liu L, Liu Y, Leng J. 4D Printing Auxetic Metamaterials with Tunable, Programmable, and Reconfigurable Mechanical Properties. Adv Funct Mater 2020;30(43):2004226. https://doi.org/10.1002/adfm.v30.4310.1002/adfm.202004226.
[26] Zhao W, Zhang F, Leng J, Liu Y. Personalized 4D printing of bioinspired tracheal scaffold concept based on magnetic stimulated shape memory composites. Compos Sci Technol 2019;184:107866. https://doi.org/10.1016/j.compscitech.2019.107866.
[27] Zhao W, Huang Z, Liu L, Wang W, Leng J, Liu Y. Porous bone tissue scaffold concept based on shape memory PLA/Fe3O4. Compos Sci Technol 2021;203:108563. https://doi.org/10.1016/j.compscitech.2020.108563.
[28] Yousuf MH, Abuzaid W, Alkhader M. 4D printed auxetic structures with tunable mechanical properties. Addit Manuf 2020;35:101364. https://doi.org/10.1016/j.addma.2020.101364.
[29] Zeng C, Liu L, Bian W, Liu Y, Leng J. 4D printed electro-induced continuous carbon fiber reinforced shape memory polymer composites with excellent bending resistance. Compos Part B: Eng 2020;194:108034. https://doi.org/10.1016/j.compositesb:2020.108034.
[30] Liu T, Liu L, Zeng C, Liu Y, Leng J. 4D printed anisotropic structures with tailored mechanical behaviors and shape memory effects. Compos Sci Technol 2020;186:107935. https://doi.org/10.1016/j.compscitech.2019.107935.
[31] Meurer J, Hniopek J, Bätz T, Zechel S, Enke M, Vitz J, et al. Shape-Memory Metallopolymers Based on Two Orthogonal Metal-Ligand Interactions. Adv Mater 2021;33(7):2006655. https://doi.org/10.1002/adma.v33.710.1002/adma.202006655.
[32] Yeo JCC, Ong XY, Koh JJ, Kong J, Zhang X, Thitsartarn W, et al. Dual-Phase Poly(lactic acid)/Poly(hydroxybutyrate)-Rubber Copolymer as High-Performance Shape Memory Materials. ACS Appl Polym Mater 2021;3(1):389–99.
[33] Liu T, Liu L, Yu M, Li Q, Zeng C, Lan X, et al. Integrative hinge based on shape memory polymer composites: Material, design, properties and application. Compos Struct 2018;206:164–76.
[34] Zeng C, Liu L, Bian W, Leng J, Liu Y. Bending performance and failure behavior of 3D printed continuous fiber reinforced composite corrugated sandwich structures with shape memory capability. Compos Struct 2021;262:113626. https://doi.org/10.1016/j.compstruct.2021.113626.
[35] Zeng C, Liu L, Bian W, Leng J, Liu Y. Compression behavior and energy absorption of 3D printed continuous fiber reinforced composite honeycomb structures with shape memory effects. Addit Manuf 2021;38:101842. https://doi.org/10.1016/j.addma.2021.101842.

[36] Dong Ke, Ke H, Panahi-Sarmad M, Yang T, Huang X, Xiao X. Mechanical properties and shape memory effect of 4D printed cellular structure composite with a novel continuous fiber-reinforced printing path. Mater Des 2021;198:109303. https://doi.org/10.1016/j.matdes.2020.109303.

[37] Ma Q, Cheng H, Jang K-I, Luan H, Hwang K-C, Rogers JA, et al. A nonlinear mechanics model of bio-inspired hierarchical lattice materials consisting of horseshoe microstructures. J Mech Phys Solids 2016;90:179–202.

[38] Yang X, Sun Y, Yang J, Pan Q. Out-of-plane crashworthiness analysis of bio-inspired aluminum honeycomb patterned with horseshoe mesostructure. Thin-Walled Struct 2018;125:1–11.

[39] Zhang W, Zhang F, Lan X, Leng J, Wu AS, Bryson TM, et al. Shape memory behavior and recovery force of 4D printed textile functional composites. Compos Sci Technol 2018;160:224–30.